analytical chemistry

Article

Consensus Receptor-Binding Domain-Targeted Aptamer Selection and Designing of a Photonic Crystal-Decorated Aptasensor for SARS-CoV-2

Ghulam Murtaza,* Aysha Sarfraz Rizvi, Min Xue, Lili Qiu, and Zihui Meng*

Cite This: *Anal. Chem.* 2022, 94, 7391−7399

Read Online

ACCESS | Metrics & More | Article Recommendations | SI Supporting Information

ABSTRACT: The frequent emergence of variants of concern (VOC) of SARS-CoV-2 necessitates a sensitive and all-inclusive detection platform that remains viable despite the virus mutations. In this context, we targeted the receptor-binding domain (RBD) of glycoprotein (S-protein) of all VOC and constructed a consensus RBD (cRBD) based on the conserved amino acids. Then, we selected a high-affinity ssDNA novel aptamer specific for the cRBD by an in silico approach. The selected aptamer is utilized to fabricate a photonic crystal (PC)-decorated aptasensor (APC-sensor), which consists of polystyrene nanoparticles polymerized within a polyacrylamide hydrogel. cRBD-responsive ssDNA aptamers are crosslinked in the hydrogel network, which selectively bind to the cRBD and SARS-CoV-2 in saliva samples. The binding response can be visually monitored by swelling of the hydrogel and color generation by diffraction of light from PCs and can be quantified by the diffraction ring diameter or a spectrometer. The sensor delivers a LOD of 12.7 ± 0.55 ng mL^{-1} for the cRBD and 3 ± 18.8 cells mL^{-1} for SARS-CoV-2 in saliva samples, with a rapid response of 5 min. The sensor can be stored and regenerated without loss of activity. It can be utilized as a point-of-care testing (POCT) for SARS-CoV-2 diagnosis.
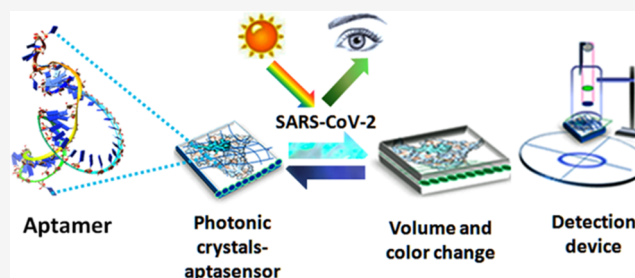
1. INTRODUCTION

The SARS-Corona viruses (SARS-CoV) have caused three major outbreaks since the beginning of the 21st century. The current SARS-CoV-2 pandemic continues to spread among humans with the appearance of several variants of concern (VOC), including alpha, beta, gamma, delta, and the recent omicron in particular, which have increased the virus transmissibility and virulence and compromised the public health measures.[1] The status quo demands massive-scale testing and diagnostics to prevent the spread of the virus. Currently available methods include the quantitative real-time polymerase chain reaction (qRT-PCR), which is a gold standard for testing of SARS-CoV-2;[2] however, it requires complex sample handling and preprocessing and might give false-negative results with the new viral mutants. Similarly, the Ig G/IgM detection also needs these antibodies to be produced by the host and achieve the required level to be tested. In addition, the required instrumentation, reagents, and skills of the operating personnel hinder their widespread use for mass testing.

Alternatively, the detection of SARS-CoV-2 through its cell surface glycoprotein (S-protein)[3−5] could be a direct way of testing the virus without the need for genetic material extraction and further processing by PCR. The virus uses the S-protein to attach to the host cells' receptors, i.e., angiotensin-converting enzyme-2 (ACE-2),[6] for infection; therefore, this feature of the S-protein can be harnessed in devising a suitable detection method. The S-protein is the target for antibodies and can be an ideal viral recognition element for direct onsite detection of the SARS-CoV-2.[7] However, most of the S-protein detection methods or sensors have relied on the use of antibodies[8−10] or ACE-2 enzymes as biorecognition elements,[11] which require animal models and a longer time for synthesis, thereby making the design of assays very expensive, and also these proteins undergo irreversible denaturation at high temperatures and pH changes.[12]

Aptamers can be an ideal and alternative choice to antibodies for the detection of the S-protein and hence the virus. They are known as chemical antibodies and are even considered superior to antibodies because their production is independent of the living host, and they are much stable and have little or no batch-to-batch variation.[13] Aptamers are single-stranded DNA (ssDNA) or RNA molecules, which are selected by the systematic evolution of ligands by exponential enrichment (SELEX) process,[14−16] and they can bind to a
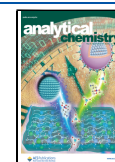
wide range of targets, including small molecules, proteins, viruses, or bacteria, with high affinity and specificity.[17,18] A few aptamers have been selected for the S-protein so far,[19] which targeted the receptor-binding (RBD) of the initial virus form, and a few sensors were developed for the detection of the S-protein based on those aptamers. The available aptamer-based sensors include aptamer-based sandwich assay,[20] electro-chemical sensors,[21] and aptamer-based immunosorbent assay (ALISA).[22] These sensing methods present good sensitivity; however, with the appearance of several VOC, including omicron, it becomes imperative to select novel aptamers, which could better target the RBD of all VOC and present a universal detection of SARS-CoV-2 despite changes or mutations in the amino acids of the S-protein in the days to come.

In this context, (i) we compared the amino acid sequence of the receptor-binding domain (RBD) of the S-protein of all VOC by multiple sequence alignment (MSA) and identified the common consensus amino acids, which are conserved among all VOC. The protein with consensus amino acids was named the consensus receptor-binding domain (cRBD). (ii) Then, we selected a high-affinity specific ssDNA aptamer for the cRBD by an in silico SELEX approach. (iii) After achieving the high affinity and specific aptamer for the cRBD, the aim was to transfer the potential of aptamer recognition capability to a point-of-care (POC) platform, which could be used as a handheld device and give optical readout signals. We utilized photonic crystals (PCs) as a sensing platform that has been successfully utilized in sensing biomolecules and cells by our research group;[23−25] however, they have not been used for the detection of SARS-CoV-2 yet. The fabrication of PCs and the relevant detection tools is as simple as that of a laser pointer, and their quantitative detection efficiency is comparable to those of the analytical instruments. Therefore, the selected aptamer was functionalized in the polyacrylamide hydrogel embedded with the PCs to synthesize a photonic crystal-decorated aptasensor (APC-sensor) for selective detection of the cRBD and SARS-CoV-2 in saliva samples. The detection could be performed with a laser pointer by measuring changes in the diffraction ring diameter upon binding to the target, and the binding event is visible to the naked eye with structural color diffraction in visible light. In addition, the sensor is compatible with an ultraviolet−visible (UV−vis) spectrometer. These features make it suitable for the development of low-cost POCT devices.

2. EXPERIMENTAL SECTION

2.1. Materials. The SARS-CoV-2 receptor-binding domain (cRBD) with consensus amino acid residues from all VOC, human serum albumin (HSA), the RBD of SARS-CoV-1, and agarose gel was purchased from Sino Biological and Sigma-Aldrich. S-proteins from all VOC were also procured from Sigma-Aldrich. The ssDNA aptamer (5′- AAAGCCACAAC-GAGCTCGGGGTGAAAGCAGTCCGTTGAG-TAGGCTTGCGGCTGCGTGGCATATCGATT-3′) and acrydite-modified ssDNA aptamer (5′-acrydite- AAAGCCA-CAACGAGCTCGGGGTGAAAGCAGTCCGTTGAG-TAGGCTTGCGGCTGCGTGGCATATCGATT -3′) were synthesized by Sangon Biotech, China. The SARS-CoV-2 pseudovirus expressing the S-protein with the cRBD and the inactivated SARS-CoV-1 and SARS-CoV-2 were obtained from YEASEN Co., Ltd. Styrene and methacrylic acid (MAA) were obtained from Aladdin. 1-(3-Dimethylaminopropyl)-3-ethyl-carbodiimidehydrochloride (EDC) was obtained from Shang-hai Medpep Co. Acrylamide (AM), 2-hydroxyethyl meth-acrylate (HEMA), potassium persulfate (KPS), N,N′-methyl-enebisacrylamide (BIS), sodium dodecyl sulfate (SDS), ethylenediaminetetraacetic acid (EDTA), dimethyl sulfoxide (DMSO), and 2,2-diethoxyacetophenone (DEAP) were obtained from Acros Organics. Saliva samples (virus-free) were obtained from healthy individuals with informed consent.

2.2. Sample Preparation. The ssDNA aptamer vials were centrifuged, and the prescribed amount of distilled water was added and dissolved to prepare 100 μM stock solutions. The stock solution was heated in a water bath at 90 °C for 3 min and cooled at room temperature to allow the aptamer to assume the desired conformation. The stock solution was stored at −20 °C until further use. The dilutions of aptamer up to 500 nM were prepared in 2 mM PBS buffer (pH 7.4). Protein stock solutions (10 μg mL^{-1}) were prepared in distilled water, and dilutions (1−1000 ng mL^{-1}) were prepared in 10 mM PBS buffer (pH 8.0). The saliva samples were obtained from individuals with informed consent under aseptic conditions. The volunteers were asked to abstain from eating and drinking for 2 h before sample collection and rinse their mouths with MilliQ water. Whole unstimulated saliva was collected directly into prechilled sterile falcon tubes and kept on ice. The whole saliva sample was diluted with distilled water (1:1 v/v) and was analyzed with or without being spiked with inactivated SARS-CoV-2 or inactivated SARS-CoV-1 at concentrations of $10^{0}−10^{8}$ cells mL^{-1}.

2.3. Amino Acid Sequence Alignment of the S-protein of VOC. The amino acid sequences of the S-protein of VOC, i.e., alpha, beta, gamma, delta, and omicron variants, were downloaded from the RCSB database (https://www.rcsb.org/) with protein databank (PDB) ID, 7FEM, 7VX1, 7SBS, 7V7N, and 7TB4, respectively. The sequences were aligned by multiple sequence alignment (MSA) on Clustal Omega (https://www.ebi.ac.uk/Tools/msa/clustalo/) web server. The conserved or consensus amino acid sequences were identified and used to construct the consensus RBD (cRBD).

2.4. In Silico SELEX. In silico SELEX is a two-step process for the screening of the sequence library. The first step is sequence testing based on the secondary structure prediction and calculation of binding free energies of secondary structures. And in the second step, virtual screening based on the minimization of energies is done to select the aptamer against the targeted protein.

2.4.1. ssDNA Library Generation. For this work, a Perl script was designed and used for the generation of an initial library of 10^{5} sequences of ssDNA. This library was screened/tested in two steps. At first, the secondary structure predictions based on stem-loop probabilities and calculations of the minimum free binding energies were made. Then, a virtual screening of structures was done to select the aptamers.

2.4.2. Secondary Structure Prediction. The initial screening of libraries was performed for cleaning the library in terms of elimination of redundant/unnecessary structures, and the generated library from the above algorithm was then used to test the structures by predicting their secondary (2D) structures on the mfold web server (http://www.unafold.org/mfold/applications/dna-folding-form.php).

For secondary structure analysis, two principles were used, i.e., "maximization and minimization of base pairs". In this work, the principle for minimization of base pairs is used for the selection of secondary structures. The stem-loop structures

were selected for further screening, and the pseudoknots (not accurate structures) were eliminated from the screening process because pseudoknots are not required for the process of virtual screening. Based on this algorithm's work, the graphical output for secondary structures was predicted in the Vienna format (dot-bracket format).

2.4.3. Tertiary Structure. Tertiary structures were built for utilization in the virtual screening process. For this purpose, the selected stable secondary structures from the first step were converted into three-dimensional (3D) structural modeling using RNAComposer (https://rnacomposer.cs.put.poznan.pl/). So, the higher interacting molecules can be selected as aptamers based on their binding free energy.

The 3D structures that were generated were further minimized using MDWeb by the process of molecular simulations. A molecular dynamics simulation was used to investigate whether the hypothetical binding conformation was stable and whether any changes occurred in the molecule. To remove extra atoms, add missing atoms, and correct coordinates and to construct the 3D structures according to in vitro structures (very near to real structures), a molecular dynamic simulation on 3D structures was performed.

2.4.4. Virtual Screening. To identify the ability of modeled DNA sequences to emerge as the cRBD aptamer, we designed an in silico approach that used these ssDNA sequences as a ligand to predict their binding with the cRBD. For this binding prediction, we used three different docking platforms, namely, the HDOCK, PatchDock, and AutoDock.

HDOCK dockings were performed on the easy interface of the server (http://hdock.phys.hust.edu.cn/) using previously prepared receptor and ligand files. HDOCK server provides user-friendly web access to the robust hybrid algorithm of template-based modeling and free docking for protein–protein and protein–DNA/RNA complexes.[26] The cRBD and ssDNA sequences were uploaded in the PDB format. Their binding residues were specified. The top ten complex models were saved as outputs.

Molecular shape complementarity docking was performed over the PatchDock web server (http://bioinfo3d.cs.tau.ac.il/PatchDock/php.php).[27] The prepared PDB files of ssDNA and cRBD were provided to the PatchDock server at a default value of 4.0 for clustering root-mean-square deviation (RMSD) and default complex type. PatchDock represents Connolly's surface of docking partners as concave, convex, and flat patches and matches them to generate candidate transformations. Auto-Dock manual program was also used for cRBD and ssDNA dockings according to the protocol described by Morris et al.[28]

The docking scores obtained in each program were used to calculate the mean-centered Z-score by the following equation, $Z = E - \overline{E}/SD$, where E is the obtained binding score of an individual mutant–protein complex (in a set of 10 best binding modes), $\overline{E}$ is the mean binding score, and SD is the standard deviation.

2.5. Gold Nanoparticle (AuNP) Affinity Assay. AuNPs were synthesized following the classical citrate reduction method.[29] Twenty-five microliters of AuNP solution was incubated with 25 μL of aptamer solution (2 μM) for 10 min in a 96-well plate. Then, 25 μL of the cRBD with different concentrations (100, 200, 400, 800 ng mL^{-1}) in PBS was added and incubated at room temperature for 15 min. Then, the color change of the AuNP solution was observed after 10 μL of NaCl solution (900 mM) was added. The absorbance at

620 and 520 nm wavelengths was recorded with a spectrometer.

2.6. Development of a Photonic Crystal-Decorated Aptasensor (APC-sensor). The aptamer with the least negative Z-score was named aptamer-1 (Apt1) and was synthesized and used to construct a photonic crystal-decorated aptasensor (APC-sensor), which consists of a photonic crystal array (PC array), produced by the self-assembly of polystyrene (PS) nanoparticles on the water surface and mounted on a glass slide and dried. The second component consists of a polyacrylamide hydrogel network, which is polymerized on the PC array and subsequently modified with Apt1. The details are described below.

2.6.1. Fabrication of Photonic Crystals. The polystyrene (PS) nanoparticles were synthesized according to the emulsion polymerization method in our laboratory.[24] The PS colloidal solution was mixed with 1-propanol (ratio 3:1 v/v) and vortexed for 1 min. Twenty microliters of this suspension was poured slowly onto the surface of pure water in a glass container (15 cm wide) using a syringe, where it formed a compact single layer with the addition of a few drops of SDS (0.01 g mL^{-1} in water). The array was gently mounted onto a clean glass slide (5 cm × 2 cm) and dried in air at room temperature. After drying, a PC array with vibrant rainbow colors was obtained.

2.6.2. Synthesis of a PC-Array-Embedded Polyacrylamide Hydrogel and Its Functionalization with an Aptamer. To synthesize the APC-sensor, a suitable concentration of AM, MAA monomers, and BIS crosslinker was mixed in as follows: 360 mg of AM, 40 μL of MAA, and 8 mg of BIS mixed in 2 mL of water. Afterward, 40 μL of DEAP solution (prepared in 10% DMSO) was added, and the mixture was deoxygenated by N$_2$ purging for 15 min.[23,30] One milliliter of this mixture was deposited on a PC array glass slide with a micropipette and covered with another glass slide, separated by a 100-μm-thick parafilm. The solution was polymerized in a UV incubator at 365 nm for 2 h. The resultant hydrogel was removed from the glass slide and then kept in 2 μM Apt1 solution prepared in 2 mM PBS buffer pH 7.4 for 24 h and then in EDC (100 μM) for 2 h to obtain an APC-sensor (Scheme 1). The APC-sensor was then washed with PBS buffer (2 mM, pH 7.4) for 2 min to remove the unreacted aptamer. The APC-sensor was equilibrated with buffer (optimized pH) to get the maximum response. All of the hydrogels were cut into small (1 cm × 1

Scheme 1. Illustration of APC-Sensor Fabrication[a]
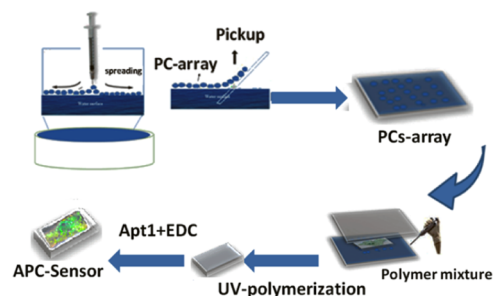
[a]Layering of the PS suspension on the surface of the water in a container and mounting onto a clean glass slide to obtain the PC array. polyacrylamide hydrogel layering on the PC array and its functionalization with Apt1 to obtain the APC-sensor.

cm) pieces before use. The nonaptamer hydrogel (NAPC-sensor) was prepared in the absence of Apt1.

2.6.3. APC-Sensor Characterization. The size of PS nanoparticles was measured with a field emission scanning electron microscope (FE-SEM, Quanta FEG 250). The surface morphology of the APC-sensor was observed through SEM images after coating a layer of gold. A iS10 Fourier transform infrared spectrometer (FTIR) was used to evaluate the incorporation of the aptamer into the hydrogel. Agarose gel electrophoresis was performed on 2% agarose gel to observe the linking of Apt1 into the hydrogel sensor by acrydite functional groups. The stability of hydrogels was evaluated with a thermogravimetric analyzer (TGA) at temperatures from 25 to 800 °C with a gradient of 10 °C/min in the presence of nitrogen gas. The amount of aptamers adsorbed into the hydrogel was found by measuring the absorbance of the aptamer in the supernatant with a double beam UV spectrophotometer at 260 nm wavelength. The protein concentrations were also determined by measuring absorbance in a UV spectrophotometer at 280 nm wavelength. The transmittance from the APC-sensor was measured with an Ocean Optics UV−vis spectrometer.

2.7. Detection of the cRBD, S-protein, and SARS-CoV-2 with the APC-Sensor. The detection was performed by immersing small pieces (1 cm × 1 cm, 100 μm thick) of APC-sensors in 200 μL solutions of cRBD (1−1000 ng mL^{-1}), S-protein of all VOC (1−1000 ng mL^{-1}), or 10^0−10^8 cells mL^{-1} of inactivated SARS-CoV-2 in Petri dishes, each for 1−10 min. The Debye diffraction ring diameter was used to measure the changes in particle spacing using a laser pointer (405 nm).[31] For this, the APC-sensors were placed underneath the laser pointer held perpendicular to the hydrogels, and diffraction rings were observed on the white screen below the hydrogels at a distance h to the hydrogels. The particle spacing of this PC array was calculated using the formula $d = 2\lambda/3 \sin \alpha$,[32] where α is the Debye diffraction's forward diffraction angle ($\alpha = \tan^{-1}(r/h)$), λ is the laser light wavelength (405 nm), d is the particle spacing, h (8.7 cm) is the distance between the PC array and the screen, and r is the radius of the Debye diffraction ring. The measurements involved only a ruler and a laser pointer.

The detection device and measurement procedure are shown in Figure S1 of the Supporting Information. The diffraction ring formation of the APC-sensor was also investigated using an Ocean Optics UV−vis spectrometer with a Tungsten Halogen light source and a fiber-optic reflection probe. APC-sensors were washed with water to remove the unbound protein in between testing different concentrations and saliva samples and subsequently washed with 10 mM Tris-HCl with 2 mM EDTA pH 7.4 to remove the bound proteins or the virus. Experiments were performed in triplicate for precision. Statistical analyses including standard deviation and comparison of means were performed using OriginPro 2019 software.

3. RESULTS AND DISCUSSION

3.1. Scheme of Work and the Operating Principle of the APC-Sensor. The outline of this work is demonstrated in Figure 1. The S-proteins of all VOC were aligned and their common/consensus amino acid sequences were determined and synthesized as the cRBD. The selected sequences of the ssDNA library were docked with the cRBD, and the finally selected Apt1 was crosslinked in the polyacrylamide hydrogel
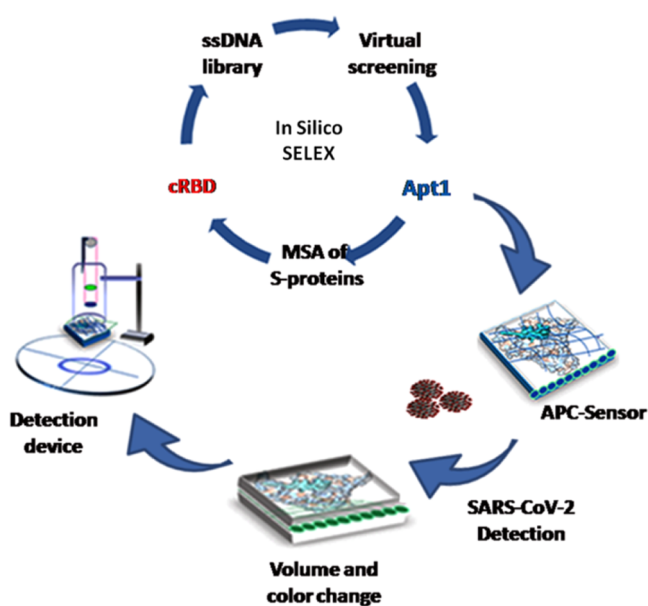

Figure 1. Illustration of the working principle of the APC-sensor. In silico SELEX provides Apt1, which is incorporated into the polyacrylamide hydrogel embedded with PCs (blue circles). The binding of the APC-sensor to either the cRBD or SARS-CoV-2 leads to a color change and swelling of the sensor.

embedded with PCs to fabricate the APC-sensor by EDC crosslinking. The aptamer has a helical structure with a stem and loop in the absence of the cRBD (Figure S2 of Supporting Information). The APC-sensor has an initial color of blue. The addition of the cRBD, S-protein, or SARS-CoV-2 carrying S-protein (on its outer surface) to the APC-sensor results in the formation of the aptamer−cRBD complex by specific hydrogen bonding, which brings a change in the conformation of the aptamer from linear to a G-quadruplex (Figure S2). This binding event can be observed as the swelling of the APC-sensor as a result of an increase in particle spacing in the PC array. A visible color change to blue-green was also observed due to a diffraction wavelength shift. The diffraction of light from the APC-sensor generates a circular ring on a white screen, which can be used to quantify the target response of the sensor.

3.2. In Silico SELEX. *3.2.1. Design of the Consensus Receptor-binding Domain (cRBD) for VOC.* MSA results of the receptor-binding domain (RBD) (V360-N540) of S-proteins from all VOC are shown in Figure S3a of the Supporting Information, which demonstrates that there are only four sites of mutation of amino acids among the latest viral mutant, i.e., omicron and other VOC. These include amino acids L-369, P-371, F-373, and A-482. The other amino acids are conserved among all five VOC. This shows the potential of the RBD for exploiting it as the leading recognition site of SARS-CoV-2. The RBD has been previously targeted as the binding site of angiotensin-converting enzyme (ACE-2)[33] and also the favorite target site for drugs and antibodies. Therefore, we found the consensus amino acid sequences among all the VOC and designed the consensus RBD (cRBD) (structure shown in Figure S2) and further evaluated it as a target for the selection of aptamers by in silico SELEX.

3.2.2. Structural Selection of cRBD Aptamer Sequences. The generation of a ssDNA library of size 10^5 and length 67 nt was based on some basic rules, i.e., maximum sequences in the

library produced stable secondary structures; the sequences have the lowest binding free energy and stem-loop distribution, which has the maximum probability of being aptamers (Figure S3b). The secondary structures were ranked based on the lowest energy (ΔG in kcal mol^{-1}), and the structures with dot-bracket notation......(((......((((....))))......))).. had a stem-loop in them. And the structures with this kind of dot-bracket notation ....[[[.{(((....(([]]...).).}.)).. had pseudoknots and were omitted in the initial screening. The selected sequences were subjected to 3D structural designing by the RNAComposer program, and the structures were saved in the PDB format for virtual screening.

3.2.3. Virtual Screening to Identify Probable Aptamers. To identify the ability of ssDNA sequences to emerge as potential aptamers, we designed a strategy to find their binding as ligands with the target cRBD. We used HDock, PatchDock, and AutoDock programs for docking. The most negative Z-score in a set of 10 best binding modes of an aptamer−cRBD complex was taken as a docking-specific Z-score of that particular complex. The total Z-score (Z_T) was computed by adding the Z-scores of HDock (ZH), PatchDock (ZP), and AutoDock (ZA), as shown in Table S1 of the Supporting Information.

The Z-score tells the strength of interactions between the aptamer and the protein target. Table S1 shows that the first five aptamer sequences showed greater interactions reflected by their lower Z-scores. The target specificity of the top five sequences was evaluated by docking with the thrombin protein (PDB id: 1PPB), and the respective Z-scores were calculated (Table S2 of the Supporting Information) and compared with the results of docking with the cRBD in Table S1.

It is evident from the Z-score results that the aptamer candidate sequences had relatively low Z-scores. For example, the Z_T of Apt1 with thrombin was −4.65, and with the cRBD, the Z_T was found to be −6.83. This suggests that the designed in silico approach of aptamer selection can selectively predict and differentiate among target-specific and nonspecific binding partners in a DNA−protein complex. Since Apt1 manifested better docking Z-scores and hence binding to the cRBD, we evaluated its binding pattern to each VOC individually and found the hydrogen bonding to be the main interaction force among amino acid residues and the Apt1 sequence, as shown in Figure 2. Figure 2a shows that a maximum number of amino acids interacting with the Apt1 are present in the RBD of the S-protein of all VOC. Therefore, it was an ideal strategy to design the aptamer targeting the RBD of the S-protein. The Z-score of Apt1 to both the RBD and the relevant S-protein of VOC (Figure 2b) reveals that Apt1 can capture the S-protein of all VOC indirectly through their RBD. Therefore, Apt1 could serve as a recognition molecule for any VOC of SARS-CoV-2. This would be useful as the Apt1 binding trend in this study shows that Apt1 would remain suitable for the detection of any upcoming mutations in the RBD/S-protein and hence the whole SARS-CoV-2.

3.3. AuNP Affinity Assay. To evaluate the recognition and specificity of Apt1, we developed a AuNP colorimetric assay, which could quickly and specifically detect its affinity and show a color reaction after binding to the target, as shown in Figure S4. AuNPs give a wine red color in a dispersion state. After the addition of NaCl, they aggregate and turn blue in color. Aptamer masks AuNPs from the effect of NaCl and shows a wine red color. After the addition of the cRBD, the aptamer binds to the cRBD, the masking effect is removed, and the
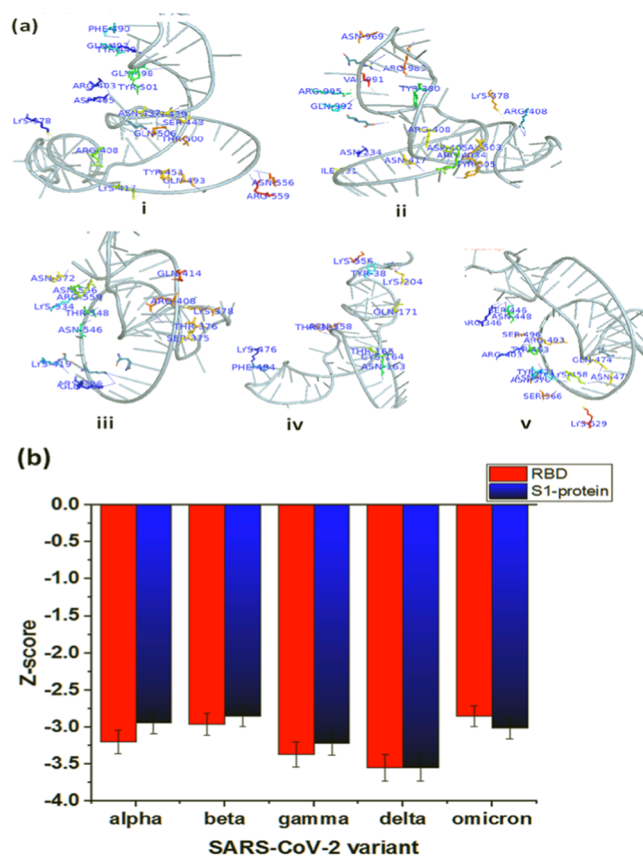

Figure 2. Interaction of Apt1 with VOC. (a) Apt1 and RBD of VOC: i, α RBD; ii, β RBD; iii, γ RBD; and iv, Delta RBD; v, Omicron RBD. (b) Relative binding Z-score of Apt1 with RBD and S-protein of VOC of SARS-CoV-2.

color changes to blue. The extent of color change is related to the concentration of the cRBD. However, the RBD of the S-protein from SARS-CoV-1 used as control did not demonstrate the color change, as shown in Figure S4a, which reveals the specificity of Apt1 for SARS-CoV-2. Apt1 demonstrated a binding constant of 0.105 μM with the cRBD (Figure S4b).

3.4. Photonic Crystal-Decorated Aptasensor (APC-Sensor). *3.4.1. Characterization of PCs and APC-Sensor.* The SEM analysis of PS nanoparticles and APC-sensor was performed to observe the size of PS nanoparticles suitable to obtain the diffraction ring diameter. The average size of PS particles effective for the diffraction ring was found to be 520 nm (Figure S5a). The PC array was assembled on the surface of the glass slide with a uniform and highly periodic structure, which remained intact during the polymerization. Figure S5b shows the APC-sensor with PS nanoparticles embedded in the polyacrylamide polymer. It can be seen that there are spaces between PS particles, where the hydrogel was formed after polymerization. The concentration of AM monomers and BIS was controlled by keeping the total monomer concentration at ~12.04% to achieve the detection of S-proteins with a molecular weight of $\cong$138 kDa without compromising the mechanical strength of the hydrogel.

The adsorption of the aptamer to the hydrogel was evaluated with a UV spectrophotometer by measuring the optical density of the supernatant solution after incubation of the hydrogel with the aptamer solution. The concentration of the original aptamer solution was 50 μg mL^{-1}. After incubating with the

aptamer solution (2 μM) for 24 h, the concentration of the aptamer in the supernatant was found to be 6.25 μg mL^{-1}. The hydrogel adsorbed 87.5% of the aptamer, which resulted in the APC-sensor (Table S3 of the Supporting Information).

The incorporation of the aptamer into the APC-sensor was also investigated by placing small pieces of the APC-sensor in the wells of agarose gel and then running the electrophoresis on 2.0% agarose gel for 40 min at 90 V. It was observed that acrydite-modified aptamers did not leave the wells and remained inside the sensor polymer (Figure 3a, lane 1,2),
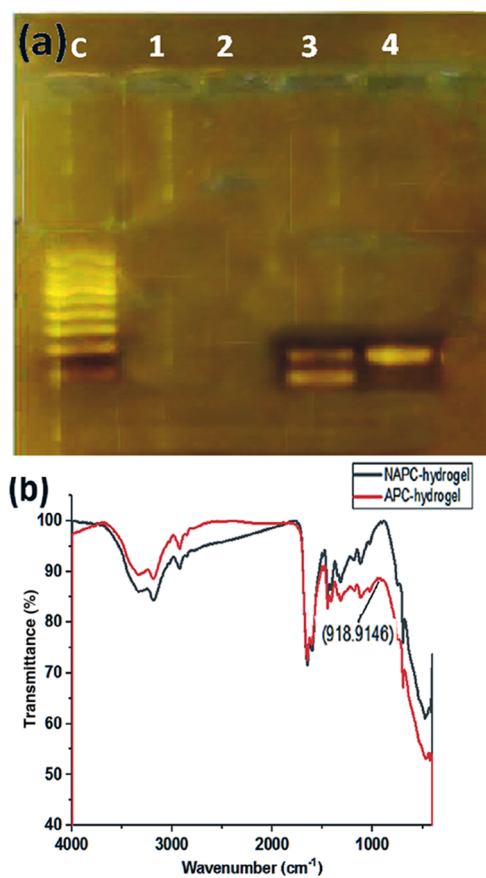

Figure 3. Aptamer linkage to the APC-sensor. (a) Qualitative analysis of aptamer incorporation. Lanes 1 and 2: APC-sensor functionalized with acrydited aptamers; lanes 3 and 4: gels containing non-acrydite-modified aptamers. C is the control DNA marker (50 bp). (b) FTIR analysis of the APC-sensor.

whereas nonmodified aptamers easily left the gel wells and were freely carried away by the running buffer (Figure 3a, lane 3,4). Further, we also confirmed the aptamer adsorption by FTIR. The spectra of the NAPC-sensor and APC-sensor are compared in Figure 3b.

The FTIR region of interest when studying aptamers is between 1800 and 600 cm^{-1}.[33] A prominent appearance of a new peak at 918 cm^{-1} shows vibrations along the sugar-phosphate backbone, resulting in the helical conformation of the nucleic acid. These bands established that the aptamer was successfully incorporated into the hydrogel. However, the structure of the hydrogel was not affected by this addition, which is confirmed by the similarity of peaks from 4000 to 1500 cm^{-1} between the APC and NAPC sensors, because the molar ratio of the aptamer to acrylamide angiotensin-converting enzyme (ACE-2)[33] was small and only about

1:2520. This also shows the smart responsiveness of the aptamer in the APC-sensor.

The thermal stability of the APC-sensor was determined by TGA, which revealed that there was a slight weight loss of 40 μg min^{-1} of the polymer film at a temperature of 100 °C and a prominent weight loss of around 200 μg min^{-1} at a temperature of 400 °C or above. So, there was no adverse effect of room temperature on the APC-sensor activity.

3.4.2. Optimizing Conditions for APC-Sensor Functioning. The effect of the pH and concentration of the buffer on the response of the APC-sensor was also evaluated (Figure S6 of the Supporting Information).

It can be seen that as the pH of blank buffer increased from 1 to 6, the hydrogel volume remained the same with 645 nm in particle spacing, with no prominent change. As the pH was further increased from 6.0 to 7.4, an increase in particle spacing from 646 to 661 nm was observed. It further increased to 723 nm at pH 8.0, and no change was observed beyond pH 8.0. The overall change in particle spacing was 77 nm (Figure S6a). This could be due to the presence of hydrophobic $-COO^-$ groups from acrylic acid, which cause the hydrogel to swell.[34]

Similarly, the concentration of the buffer was optimized by incubating APC-sensors in buffer concentrations of 2, 5, and 10 mM. The maximum particle spacing of 714 nm was obtained in the 10 mM buffer (Figure S6b). APC-sensors demonstrated the maximum response in 10 mM PBS buffer (pH 8.0) and hence used for further experiments.

3.4.3. Detection of the cRBD and S-protein of VOC by the APC-Sensor. The APC-sensor was utilized for the determination of the cRBD and S-proteins of VOC, i.e., S-α, S-β, S-γ, S-delta, and S-Omicron (concentration range 1−1000 ng mL^{-1}) to evaluate the performance of the sensor. The particle spacing of the APC-sensor increased from 646 to 742 nm with the cRBD with a net change of 142 nm in particle spacing (Figure 4a), resulting in hydrogel swelling from 1 to 25% (Figure S7 of the Supporting Information), along with the visible color change from yellow-green to blue-green (Figure 4a).

The intensity of color change increased with the increasing concentration of the cRBD within 5 min, which is the direct way for the determination of cRBD. S-proteins were also detected with a particle spacing change response of 105 nm for S-α and S-β, 104 nm for S-γ, 108 nm for S-delta, and 100 nm for S-Omicron (Figure 4a), which is comparatively lower than that observed with the cRBD. This different response could be due to the larger size of S-proteins (131.79−144.88 kDa) than that of the cRBD (19.07 kDa). The binding response was further investigated by calculating the binding affinity of Apt1 in the APC-sensor for the cRBD and S-proteins, which revealed different binding affinities (K_b) toward the cRBD and each of the S-protein (Table S4 of the Supporting Information), and this feature could also be used for the differentiation of VOC with the proposed sensor. The APC-sensor also exhibited good selectivity when tested against the S-protein of SARS-CoV-1/SARS-CoV,[35] where only a shift of 18 nm in particle spacing and no prominent color change was observed (Figure 4a). This could be due to the difference in the sequence of amino acids in the receptor-binding motif of two viruses.[36]

The particle spacing change obtained from diffraction rings with a laser pointer was compared with the transmittance obtained from a UV−vis spectrometer for the cRBD. The intensity increased from 85.55 to 221.18% with an increasing
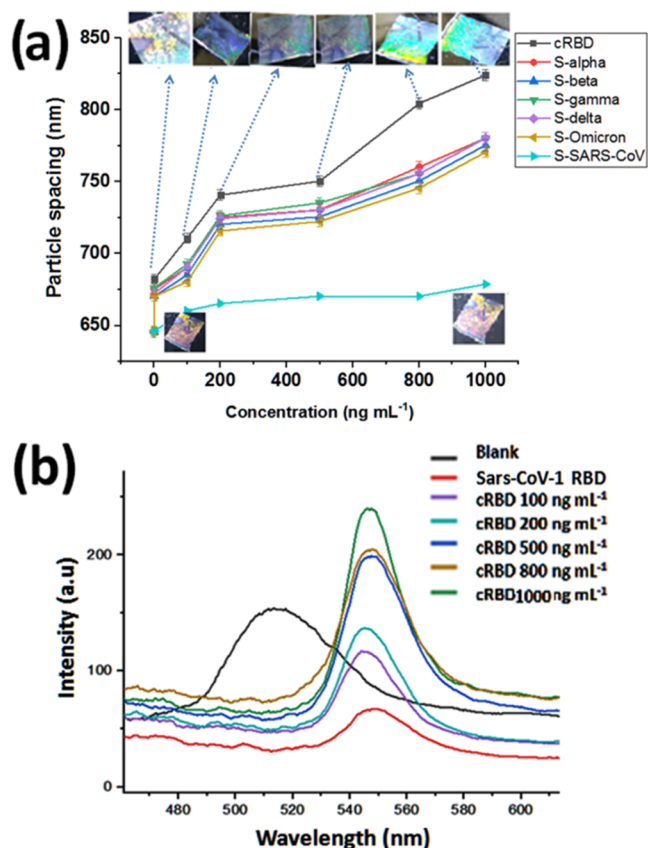
Figure 4. Determination of the cRBD and S-proteins of VOC by the APC-sensor, where S−SARS-CoV is the control tested at 500 ng mL^{-1} concentration. (a) Particle spacing measurements with the Debye diffraction ring diameter obtained with a laser pointer. (b) Measurements of the cRBD from the APC-sensor using a UV−vis spectrometer. SARS-CoV-RBD was tested as a control at 500 ng mL^{-1} concentration.

the spectrometer has a limitation in the wavelength range. Contrarily, Debye ring diffraction measurement is simple, convenient, and cheap. The analyte concentration can be determined with only a ruler and laser pointer, and no careful handling of light is required.

3.5. Reversibility and Reusability. The reversibility/reusability of the APC-sensor was also evaluated by measuring changes in the Debye diffraction ring when alternatively sensing 500 ng mL^{-1} RBD and then washing off the protein with 10 mM Tris-HCl 2 mM EDTA (pH 7.4) after usage. Figure S8a in the Supporting Information shows that the response of the APC-sensor was reversible five times. The sensor reversibility in terms of its adsorption efficiency was compared with a fresh APC-sensor from the same batch of material. The ANOVA test at a 0.05 level revealed that the means of the adsorption efficiency were not significantly different (Figure S8b). The sensor maintained its adsorption up to 70% in its fifth use as compared with the control.

3.6. Determination of SARS-CoV-2 from Saliva Samples. Rapid, convenient, and direct detection of the whole coronavirus is essential for timely diagnosis and subsequent treatment. Our developed APC-sensor can detect different concentrations of the whole SARS-CoV-2 from saliva samples without any genetic extraction, which saves time and labor.

The Apt1 in the APC-sensor can sensitively bind to the surface S-protein of SARS-CoV-2 through the RBD. The sensor exhibited obvious color and particle spacing change, which could be measured through the diffraction ring diameter (Figure 5a). The sensor delivered a wide linear detection range (10^0-10^8 cells mL^{-1}) ($y = 16.39x + 906.9$) and $R^2 = 0.983$ for the SARS-CoV-2 pseudovirus with a shift of 130 nm in particle spacing from 915 to 1045 nm and a LOD of 3 ± 18.8 cells mL^{-1} (calculated from the curve using the formula LOD = 3 × SD/slope, where SD is the standard deviation of the response). The UV−vis spectrometer reflection spectra are shown in Figure 5b; the intensity of the signal increased from 459 to 791 a.u. with a net change of 331 a.u intensity. To further prove that the cRBD-targeted APC-sensor is an efficient detection system for the SARS-CoV-2, we also tested the heat-inactivated SARS-CoV-2 in the same concentration range, i.e., (10^0-10^8 cells mL^{-1}) ($y = 13.27x + 905.3$, $R^2 = 0.921$) and found that the APC-sensor was equally effective and could

concentration of the cRBD (1−1000 ng mL^{-1}) (Figure 4b), which is comparable to the diffraction measured from the Debye diffraction diameter. NAPC-sensor did not show a significant response to either cRBD or RBD of SARS-CoV. The measurement of diffraction spectra with a spectrometer is expensive and needs careful handling of incident light. Also,
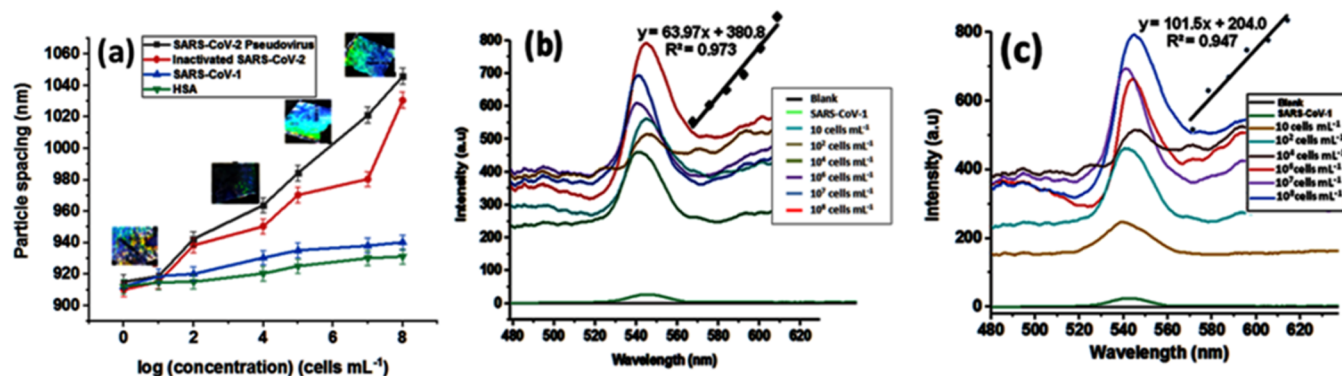

Figure 5. Determination of SARS-CoV-2 from saliva samples. (a) Detection of the SARS-CoV2 pseudovirus and inactivated virus and selectivity against SARS-CoV-1 and HSA by the APC-sensor as observed by the diffraction of laser light and Debye ring measurement. (b) UV−vis spectrometer measurements of the SARS-CoV-2 pseudovirus at concentrations of 10^0-10^8 cells mL^{-1}. UV−vis spectrometer measurements of (b) SARS-CoV-2 pseudovirus and (c) inactivated SARS-CoV-2 at concentrations of 10^0-10^8 cells mL^{-1}. SARS-CoV-1 (10^4 cells mL^{-1}), HSA 500 ng mL^{-1}. Error bars represent the SD of samples ($n = 3$).

provide visual detection with a shift of 120 nm change (Figure 5a), which was comparable to the 130 nm change observed with the pseudovirus, and also delivered a LOD of 5 ± 18.8 cells mL^{-1}.

The peaks obtained with a UV–vis spectrometer are also shown in Figure 5c, which demonstrate a net change of 543 a.u. in signal intensity from 244 to 787 a.u. The response obtained for inactivated SARS-CoV-2 with a UV–vis spectrometer is, therefore, greater than that obtained for the SARS-CoV-2 pseudovirus, which shows the enormous potential of the APC-sensor for SARS-CoV-2 detection. The sensor exhibited selectivity against a similar virus, i.e., SARS-CoV-1, with only a shift of 28 nm in particle spacing (Figure 5a), and a negligible signal response from a UV–vis spectrometer at a concentration of 10^4 cells mL^{-1}.

The presence of salivary protein, albumin, might interfere with the detection of the S-protein or SARS-CoV-2 as a whole; therefore, we tested human serum albumin with the APC-sensor, which demonstrated a shift of 19 nm in particle spacing (Figure 5a). Therefore, we did not observe any significant interference by similar proteins and similar viruses, and SARS-CoV-2 was detected with an obvious color change and particle spacing change.

3.7. Comparison of the APC-Sensor with Contemporary Methods. Our sensor is selective for all VOC of SARS-CoV-2 and does not require antibodies and virus pretreatment. It utilizes a more stable ssDNA cRBD aptamer and offers an enclosed and protected environment for the aptamer to operate, giving a visual readout with a pronounced color change upon interaction with the cRBD. No complex instrument is required either, yet it delivers rapid and quantitative detection with the output visible to the naked eye. In addition, the sensor can be stored at 4 °C in a dry form for a longer time and regenerated for use. A comparison of the efficiency of the APC-sensor with contemporary sensing methods is presented in Table S5 of the Supporting Information.

4. CONCLUSIONS

We have presented ssDNA aptamer selection by in silico approach specifically targeting the consensus receptor-binding domain of the S-protein of SARS-CoV-2 VOC. This approach provided a universal aptamer for all existing VOC, and based on the binding trend of Apt1 in the APC-sensor with the S-proteins of VOC, it is foreseen that it would be effective for the detection of any upcoming anticipated virus mutations. The designed sensor carries the advantages of specific and reversible binding to the cRBD, better storage and protection of the aptamer from the environment, and gives manifold repeatability. cRBD detection is rapid and convenient, which utilizes the changes in the diffraction ring diameter upon addition of the SARS-CoV-2 to the samples and also the visible color change within a short time of 5 min. Photonic crystals provide excellent signal reporting and enhance the sensitivity of the sensor. APC-sensor possesses features of a good sensor that can selectively detect SARS-CoV-2 without any interference from similar viruses and proteins in saliva samples. It is simple, handheld, and repeatable; however, biosafety should be considered while testing and regenerating the sensor for repeated usage. The sensor gives a new approach to the POCT of SARS-CoV-2.

■ ASSOCIATED CONTENT

ⓈⒾ Supporting Information

The Supporting Information is available free of charge at https://pubs.acs.org/doi/10.1021/acs.analchem.2c00937.

The experimental setup, a table for Z-score of the aptamer, selectivity, a table for the aptamer and adsorption, analytical performance, comparison of POCT methods, and the Figures for MSA analysis, AuNPs assay, SEM images, optimization of pH, and swelling ratio of the APC-sensor, and Figures for reusability of the sensor (PDF)

■ AUTHOR INFORMATION

Corresponding Authors

Ghulam Murtaza − *School of Chemistry and Chemical Engineering, Beijing Institute of Technology, Beijing 100081, China*; Email: murtazascholar@bit.edu.cn

Zihui Meng − *School of Chemistry and Chemical Engineering, Beijing Institute of Technology, Beijing 100081, China*; ⓘ orcid.org/0000-0002-2751-0057; Phone: 0086-13718585627; Email: mengzh@bit.edu.cn

Authors

Aysha Sarfraz Rizvi − *School of Chemistry and Chemical Engineering, Beijing Institute of Technology, Beijing 100081, China*

Min Xue − *School of Chemistry and Chemical Engineering, Beijing Institute of Technology, Beijing 100081, China*; ⓘ orcid.org/0000-0001-9786-8225

Lili Qiu − *School of Chemistry and Chemical Engineering, Beijing Institute of Technology, Beijing 100081, China*

Complete contact information is available at:
https://pubs.acs.org/10.1021/acs.analchem.2c00937

Author Contributions

The manuscript was written with the contributions of all authors. All authors have approved the final version of the manuscript.

Notes

The authors declare no competing financial interest.

■ ACKNOWLEDGMENTS

■ REFERENCES

(1) Choi, J. Y.; Smith, D. M. *Yonsei Med. J.* **2021**, *62*, 961−968.

(2) Wang, W.; Xu, Y.; Gao, R.; Lu, R.; Han, K.; Wu, G.; Tan, W. *JAMA* **2020**, *323*, 1843−1844.

(3) Mason, R. J. *Eur. Respir. J.* **2020**, *55*, No. 2000607.

(4) Rockx, B.; Kuiken, T.; Herfst, S.; Bestebroer, T.; Lamers, M. M.; Oude Munnink, B. B.; de Meulder, D.; van Amerongen, G.; van den Brand, J.; Okba, N. M. A.; Schipper, D.; van Run, P.; Leijten, L.; Sikkema, R.; Verschoor, E.; Verstrepen, B.; Bogers, W.; Langermans, J.; Drosten, C.; Fentener van Vlissingen, M.; Fouchier, R.; de Swart, R.; Koopmans, M.; Haagmans, B. L. *Science* **2020**, *368*, No. eabb7314.

(5) Walls, A. C.; Park, Y. J.; Tortorici, M. A.; Wall, A.; McGuire, A. T.; Veesler, D. *Cell* **2020**, *181*, 281−292.e6.

(6) Raghuvamsi, P. V.; Tulsian, N. K.; Samsudin, F.; Qian, X.; Purushotorman, K.; Yue, G.; Kozma, M. M.; Hwa, W. Y.; Lescar, J.; Bond, P. J.; Macary, P. A.; Anand, G. S. *eLife* **2021**, *10*, No. e63646.

(7) Ou, X.; Liu, Y.; Lei, X.; Li, P.; Mi, D.; Ren, L.; Guo, L.; Guo, R.; Chen, T.; Hu, J.; Xiang, Z.; Mu, Z.; Chen, X.; Chen, J.; Hu, K.; Jin, Q.; Wang, J.; Qian, Z. *Nat. Commun.* **2020**, *11*, No. 1620.

(8) Li, Y.; Peng, Z.; Holl, N. J.; Hassan, M. R.; Pappas, J. M.; Wei, C.; Izadi, O. H.; Wang, Y.; Dong, X.; Wang, C.; Huang, Y. W.; Kim, D.; Wu, C. *ACS Omega* **2021**, *6*, 6643−6653.

(9) Santis, R.; De; Fillo, S.; Luca, V.; Faggioni, G.; Amore, N. D.; Regalbuto, E.; Salvatori, P. *Biosens. Bioelectron.* **2020**, *171*, No. 112686.

(10) Seo, G.; Lee, G.; Kim, M. J.; Baek, S.; Choi, M.; Ku, K. B.; Lee, C.; Jun, S.; Park, D.; Kim, H. G.; Kim, S.; Lee, J.; Kim, B. T.; Park, E. C.; Kim, S. Il. *ACS Nano* **2020**, *14*, 5135−5142.

(11) Mavrikou, S.; Tsekouras, V.; Hatziagapiou, K.; Tsalidou, A.; Bakakos, P.; Rovina, N.; Koutsoukou, A.; Michos, A.; Nikola, O.; Koniari, E.; Papaparaskevas, J.; Chrousos, G. P.; Kanaka-Gantenbein, C.; Kintzios, S. *Chemosensors* **2021**, *9*, 341.

(12) Dhar, P.; Samarasinghe, R. M.; Shigdar, S. *Int. J. Mol. Sci.* **2020**, *21*, 2485.

(13) Sun, H.; Zu, Y. *Molecules* **2015**, *20*, 11959−11980.

(14) Tuerk, C.; Gold, L. *Science* **1990**, *249*, 505−510.

(15) Kinghorn, A. B.; Fraser, L. A.; Tanner, J. A.; et al. *Int. J. Mol. Sci.* **2017**, *18*, 2516.

(16) Ahirwar, R.; Nahar, S.; Aggarwal, S.; Ramachandran, S.; Maiti, S.; Nahar, P. *Sci. Rep.* **2016**, *6*, No. 21285.

(17) Bai, H.; Wang, R.; Hargis, B.; Lu, H.; Li, Y. *Sensors* **2012**, *12*, 12506−12518.

(18) Ramlal, S.; Mondal, B.; Lavu, P. S.; Bhavanashri, N.; Kingston, J. *Int. J. Food Microbiol.* **2018**, *265*, 74−83.

(19) Song, Y.; Song, J.; Wei, X.; Huang, M.; Sun, M.; Zhu, L.; Lin, B.; Shen, H.; Zhu, Z.; Yang, C. *Anal. Chem.* **2020**, *92*, 9895−9900.

(20) Svobodova, M.; Skouridou, V.; Jauset-rubio, M.; Vi, I.; Fern, A.; Julio, J.; Alvargonzalez, C.; Poveda, E.; Benavent, C.; Sans, T.; Bashammakh, A.; Alyoubi, A. O.; Sullivan, C. K. O. *ACS Omega* **2021**, *6*, 35657−35666.

(21) Idili, A.; Parolo, C.; Alvarez-Diduk, R.; Merkoçi, A. *ACS Sens.* **2021**, *6*, 3093−3101.

(22) Gupta, A.; Anand, A.; Jain, N.; Goswami, S.; Anantharaj, A.; Patil, S.; Singh, R.; Kumar, A.; Shrivastava, T.; Bhatnagar, S.; Medigeshi, G. R. *Mol. Ther. − Nucleic Acids* **2021**, *26*, 321−332.

(23) Xue, F.; Meng, Z.; Wang, F.; Wang, Q.; Xue, M.; Xu, Z. *J. Mater. Chem. A* **2014**, *2*, 9559−9565.

(24) Rizvi, A. S.; Murtaza, G.; Yan, D.; Irfan, M.; Xue, M.; Meng, Z. H.; Qu, F. *Talanta* **2020**, *208*, No. 120403.

(25) Murtaza, G.; Rizvi, A. S.; Irfan, M.; Yan, D.; Khan, R. U.; Rafique, B.; Xue, M.; Meng, Z. H.; Qu, F. *Anal. Chim. Acta* **2020**, *1117*, 1−8.

(26) Yan, Y.; Zhang, D.; Zhou, P.; Li, B.; Huang, S.-Y. *Nucleic Acids Res.* **2017**, *45*, W365−W373.

(27) Schneidman-Duhovny, D.; Inbar, Y.; Nussinov, R.; Wolfson, H. J. *Nucleic Acids Res.* **2005**, *33*, W363−W367.

(28) Morris, G. M.; Huey, R.; Olson, A. J. *Curr. Protoc. Bioinf.* **2008**, 1−40.

(29) Liu, J.; Lu, Y. *Nat. Protoc.* **2006**, *1*, 246−252.

(30) Wang, Y.; Xie, T.; Yang, J.; Lei, M.; Fan, J.; Meng, Z.; Xue, M.; Qiu, L.; Qi, F.; Wang, Z. *Anal. Chim. Acta* **2019**, *1070*, 97−103.

(31) Cai, Z.; Luck, L. A.; Punihaole, D.; et al. *Chem. Sci.* **2016**, *7*, 4557−4562.

(32) Zhang, J.-T.; Chao, X.; Liu, X.; Asher, S. A. *Chem. Commun.* **2013**, *49*, 6337−6339.

(33) *Encyclopedia of Analytical Chemistry*; John Wiley&Sons Ltd.: Chichester, 2006. DOI: 10.1002/9780470027318.

(34) Martínez-Ruvalcaba, A.; Becerra-Bracamontes, F.; Sánchez-Díaz, J. C.; González-Álvarez, A. *Polym. Bull.* **2009**, *62*, 539−548.

(35) Sun, C.; Chen, L.; Yang, J.; Luo, C.; Zhang, Y.; Li, J.; Yang, J.; Zhang, J.; Xie, L.; Protein, A. B. SARS-CoV-2 and SARS-CoV Spike-RBD Structure and Receptor Binding Comparison and Potential Implications on Neutralizing Antibody and Vaccine Development. *Biorxiv* DOI: 10.1101/2020.02.16.951723.

(36) Rossi, G. A.; Sacco, O.; Mancino, E.; Cristiani, L.; Midulla, F. *Infection* **2020**, *48*, 665.